Qualification of an Automatic Laser Beam Focus Monitoring Implemented on a New Ultrashort Pulsed Laser Robot System

Yongting Yang*1, Daniel Franz1, Elias Coulon1, Cemal Esen2, and Ralf Hellmann1

¹Applied Laser and Photonics Group, University of Applied Sciences Aschaffenburg, Würzburger Straße 45, Aschaffenburg, 63743, Bavaria, Germany

²Applied Laser Technologies, Ruhr University Bochum, Universitätsstraße 150, Bochum, 44801, Nordrhein-Westfalen, Germany

*Corresponding author's e-mail: Yongting.Yang@th-ab.de

We report on an automatic laser beam focus monitoring approach for an ultrashort pulsed laser robot system. The system integrates an ultrashort laser mounted on a link of a six-axis industrial articulated robot with a galvanometer scanner and an F-Theta lens mounted on the end of the last robot axis. This enables high precision micromachining using ultrashort pulsed laser over a large 3D processing area. A beam focus monitoring and adjustment method combining a distance sensor and cameras ensures consistent processing quality during extensive robot movement. A conventional beam focus monitoring algorithm based on image processing is compared with a deep learning-based method using YOLO object detection network, where a high accuracy is particularly observed using YOLO network-based method. In addition, the methods are implemented in the system and utilized for the beam focus monitoring for an ablation process of fused silica, with varying the processing surface orientations. Both methods demonstrate the capability for a correct beam focus detecting with surface orientations ranging from -30° to 15°, while maintaining the beam propagating axis parallel to the surface normal.

DOI: 10.2961/jlmn.2026.01.2001

Keywords: ultrashort pulsed laser, laser robot, process monitoring, 3d micromachining, YOLO object detection application

1. Introduction

Ultrashort pulsed (USP) lasers with their nonlinear material-radiation interaction mechanisms, such as multiphoton absorption and avalanche ionization have been intensively studied in medical applications [1, 2], scientific research [3, 4] and industry [5, 6]. In comparison to conventional long-pulse lasers, USP lasers have pulse durations in the picosecond and femtosecond range, which is typically shorter than the thermal conduction timescale. This minimizes thermal effects and damage to the surrounding material during laser material processing. Additionally, small beam spots enable high-precision micromachining. These characteristics make USP lasers essential for micro and nanoscale processing of sensitive materials, such as, e.g., semiconductor [7], dielectrics [8] and insulating materials [9, 10].

Due to the nonlinear interaction mechanisms, USP laser processing exhibits a high sensitivity on beam focus position. For example, in two-photon polymerization, precise control of beam focus is essential to expose the resin selectively and form the designed structure accurately, as the two photon absorption process initiates only when the exposure dose exceeds a specific polymerization threshold [11]. In direct wave guide writing [12], 3D wave guide structures are directly modified in a transparent substrate by accurately positioning the beam focus at the desired location in the material. Focusing the beam on the backside of the transparent material facilitates a so-called bottom-up machining

approach, which enhances process capability and quality [13, 14]. Additionally, precise beam focusing positioning plays also a role in conventional top-down processes. A shift in the beam focus increases the beam diameter on the substrate surface, resulting in a reduction of fluence, which in turn, leads to a low ablation depth while maintaining constant beam pulse energy. However, with remaining the same fluence, the ablation rate is improved using a defocused beam [15, 16].

To ensure process accuracy, a variety of sensors are employed for the purpose of monitoring and adjusting the laser beam focus during USP laser processing.

Acoustic and optical microphones are typical sensors used for real-time focus position adjustment, since the generated acoustic emissions during laser processing depend sensitively on the beam focus position. The correlation between the beam focus and acoustic emission is consequently applied to ascertain the position of the beam focus during the process [17].

In the context of rapid advancements in image sensing and processing technologies, also cameras have been used in in-situ laser focus adjustment. Cao et al°[18] separated the laser beam using a two-holes mask and determined beam focus position through measuring the beam spot spacing using cameras. Based on the captured spot spacing, the defocused beam was then corrected by a three-lens focus shifting system. In addition, the same research group applied a CCD camera to capture the reflection of the beam spot from a

tilted surface. The defocused beam exhibited a comma shape on the sensor, while the beam assumed an ellipse form as the beam was focused on the surface [19].

Du et. al [20] determined the beam focus using a quarter circular knife and an annular diffractive optical element. The generated beam shapes were captured by a CCD camera, where the circular form indicated that the beam was focused on the surface. The system achieved a detection accuracy of 100 nm within a range of $76 \mu \text{m}$.

During the last decades, artificial intelligence has played an increasingly important role across various fields, particularly in object detection and classification. [21, 22]. In particular, YOLO (You Only Look Once) [23] has been widely used in real-time applications due to its efficiency in object detection. Jiang et al. [24] developed a lightweight model based on YOLO-V4 model, reducing the number of parameters to one-tenth of the original model. This optimization significantly enhanced training and prediction efficiency. The model with one third of the original training time achieved a precision of 92%, which is only 4% lower than the original model for a real-time ship detection. Zhou [25] developed an enhanced model YOLO-NL (You Only Look Once and None Left) based on YOLOX. The model with the improved CSPNet (Cross Stage Partial Network), a new SSPP (Serial Spatial Pyramid Pooling network) and the optimized PANet exhibited a 2.64% improvement in mAP (mean Average Precision) as well as a higher detection efficiency compared to the original model for a real-time face mask detection.

Recently, the authors introduced an ultrashort pulsed laser robot (USPLR) system for large area 2D and 3D micromachining [26, 27]. The USP-laser is integrated into one link of a six-axis industrial articulated robot. The laser beam is guided by optical components along the robot axes arriving at the last axis, on which a scanner consisting of two galvanometer deflectors and an F-Theta are mounted for the processing. In such an approach, an automatic focus monitoring before and during the process with substantial robot 3D movements is essential to maintain the processing precision using USPLR system. However, the current existing beam

focus monitoring methods rely on a stable positioning of sensors and are suitable only for the laser source without movement during the process. In addition, YOLO models with high detection efficiency and tolerance of environmental deviation show potential for enhancing the accuracy of beam focus monitoring for the USPLR system. Thus, a flexible focus monitoring and adjustment approach for 3D processing using the USPLR system is discussed in this contribution.

The system structure as well as the beam guidance is illustrated in section 2. The beam focus monitoring and adjustment method is described in section 3. For focus monitoring using USPLR system, a conventional image processing-based algorithm is compared with a deep learning-based YOLO object detection model in section 4. Subsequently, an ablation on fused silica with various surface orientations is discussed.

2. Experimental

As illustrated in Fig. 1, the USPLR system is composed primarily of a six axis industrial articulated robot (IRB 2600ID-8/2.00, ABB) and a 1030 nm USP laser (CB3-40W, Light Conversion) mounted between Axis3 and Axis4. The laser beam guided by mirrors propagates along the subsequent robot axes. After arriving at Axis6, the laser beam is deflected and focused by a scanner consisting of two 2D galvanometer deflectors (RTAX-A15 and RTAY-A15, Newson) and a telecentric F-Theta lens with a focal length of 160 mm (JENar Silverline F-Theta, Jenoptik). A cascade beam stabilization system is integrated into the USPLR system. Each stage of stabilization system consists of two cameras and two mirrors, in which the mirror is aligned by a piezoelectrical inertial actuator (PIAK10, Thorlabs) pair in the x and y direction according to the beam position captured by the camera. The first stage consists of M1 and M2 as well as Cam1 and Cam2 (2x DMK 37AUX250, The Imaging Source), M5 and M6 as well as Cam3 and Cam4 (2x DMK 38UX541, The Imaging Source) contribute to the second stage. Beam stabilization subpresses the beam misalignment and ensures a high overlap of the current beam alignment to

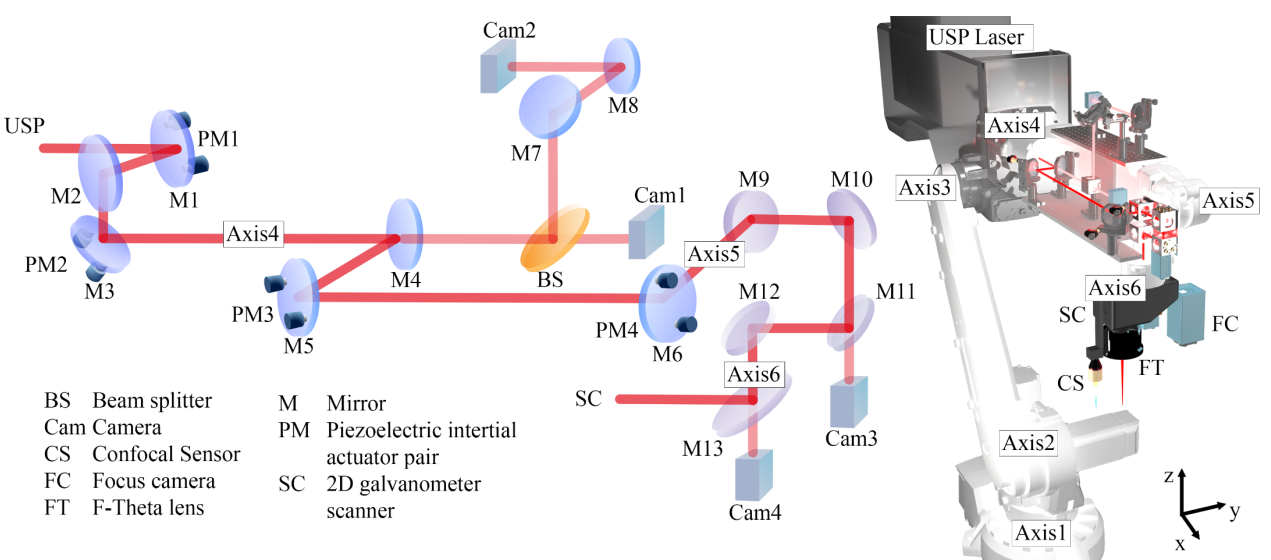


Fig. 1 Illustration of the USPLR system. An USP laser is fixed on the robot between Axis3 and Axis4. The laser beam is guided by mirrors, propagating cross axes as well as a 2D galvanometer scanner and an F-Theta lens mounted on Axis 6. A confocal sensor and a camera mounted on Axis6 are used for beam focus monitoring.

the optimal beam alignment propagating cross robot axes during the 3D processing. This limits total beam deviation of both cameras to under 55 μ m (further details are published in Ref. [28]).

Round polished fused silica (En08, GVB solutions in glass) specimens with a diameter of 26.8 mm and thickness of 9.2 mm were applied for a 2×2 mm square cavity ablation in the experiment. A pulse duration of 239 fs, a repetition rate of 200 kHz and a fluence of 2.49 J/cm² were used in the ablation process. The beam diameter was measured in 64 μ m (1/e²). A cavity is ablated by 30 laser passes. In each laser pass, the scanner deflects beam along hatch lines, remaining a constant beam spot overlap of 75% along and between the hatch lines. Additionally, a rotation of 100° on hatch line direction between each layer pass ensures a homogeneous ablation process. The ablation depth and the average surface roughness R_a were measured by a laser scanning microscope (LSM VK-X3000, Keyence).

3. Method

3.1 Focus monitoring on the USPLR system

Precise beam focus positioning ensures the quality of the laser process with substantial robot movements in the 3D processing area. Using the USPLR system, the laser propagating axis behind the F-Theta lens remains parallel to the normal of processing surface during the 3D process, which thus avoids the inhomogeneous fluence distribution and enhances process efficiency.

The focus monitoring method is shown in Fig. 2. The movement of the robot system between confocal sensor, scanner and camera remains parallel to the processing surface. In another word, the beam propagating axis behind F-Theta lens is parallel to the processing surface normal during the movement. The focus adjustment for the initialization of the process consists of three steps:

- 1. The robot adjusts the distance between F-Theta lens and processing surface using a confocal sensor (CL-L070, Keyence). The confocal sensor remains parallel to the processing surface normal. (Fig. 2(a)).
- 2. A mask is written by laser for the set distance adjustment. Each mark in the mask represents an offset step and is written using laser after robot moved one offset step along the surface normal. A mask is completed once the robot moves across the entire offset range. (as illustrated in Fig. 2(b)). The negative offset means the distance between F-Theta lens and processing surface

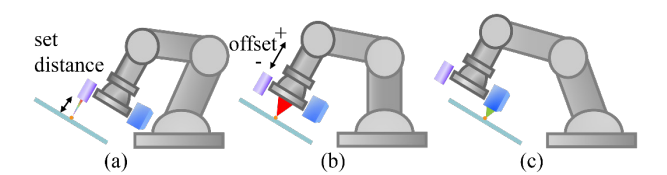


Fig. 2 Beam focus monitoring and adjustment steps of USPLR system. (a) Robot moves the confocal sensor to the processing area and adjusts the distance between specimen surface and F-Theta lens along the processing surface normal. (b) A mask for set distance adjustment is written using laser. Robot moves F-Theta lens along the surface normal across an offset range. (c) Robot moves camera to the location of processed mask remaining the camera sensor parallel to the processing surface. The current focus is analyzed and the set distance for the confocal sensor is corrected subsequently.

Table 1 Technical specifications of USPLR system.

	unit	value
Robot position accuracy	mm	0.033
Robot line path accuracy	mm	0.7
Zoom camera resolution	μm/pixel	8
Confocal sensor resolution	μm	0.25

reduces and positive offset represents the increase on the distance between F-Theta lens and processing surface

3. A camera with zoom adjustment function (DMK 39GX548-Z20, The Imaging Source) is mounted on Axis6 for recording the laser mask (Fig. 2(c)). A high resolution is extended by using a macro lens (Achromatic +10, SAGA). Robot moves camera to the position of the processed mask. The current beam focus position is analyzed, and the set distance for the confocal sensor is updated.

Please note that step 1 is utilized to regulate the distance between F-Theta lens and processing surface not only prior to the initiation of the process but also during the process periodically. The technical specifications of the USPLR system are shown in Table. 1.

3.2 Beam focus position determination

The mask applied for beam focus position monitoring in the experiment is illustrated in Fig. 3. Maintaining the beam propagating axis parallel to the surface normal, the robot moves along the surface normal across the entire distance offset range of ±2 mm from the set distance with an offset step of 200 µm. One laser mark as well as two extra direction marks on both sides are written by the laser after the robot arrives on the corresponding offset, wherein the large central mark denotes the defined set distance. Negative offsets are indicative of a decrease in the distance between the F-Theta lens and the processing surface, while positive offsets indicate an increase in distance. Since visible marks beyond the offset range result in a wrong calculation of the beam focus, a low laser fluence slightly beyond the threshold is required for the mask writing, with which only a part of marks is visible while ensuring the mark next to the direction mark invisible. The current beam focus is therefore determined as

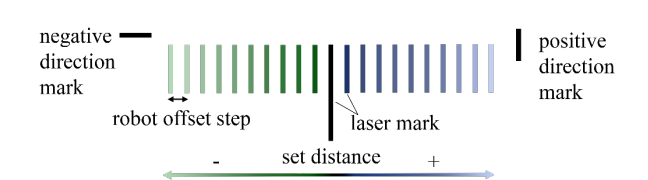


Fig. 3 Mask for beam focus monitoring and set distance adjustment. Marks are written by the laser and scanner. One mark represents an offset step and is written after robot moves one offset step along the processing surface normal. The large central mark represents the defined set distance, where the offset is 0. Two direction mark reveal the robot offset direction.

the corresponding offset represented by the center of the visible marks.

The center of the visible marks is calculated by

$$N_{center} = (N_p + N_n)/2, \tag{1}$$

where the $N_p > 0$, $\forall N_p$ is the mark number in positive direction and $N_n < 0$, $\forall N_n$ is the number of marks in the negative direction. If the N_{center} is smaller than 0, the current focus is above the processing surface and the set distance of confocal sensor should be decreased. In contrast, the set distance should be increased for $N_{center} > 0$. The value of N_{center} indicates the number of offset increments that should be appended on the set distance. A correct focus position is observed by $N_{center} = 0$.

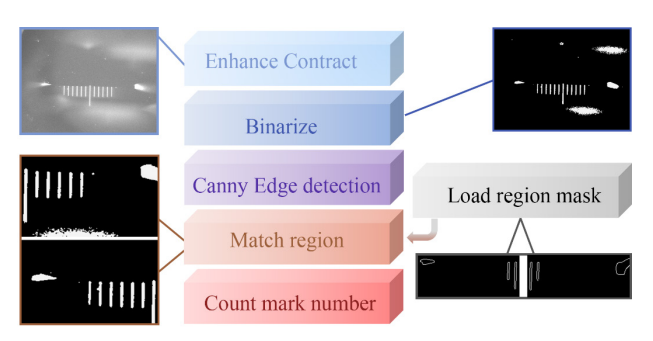


Fig. 4 Image processing for beam focus determination. The contour of visible marks is determined using Canny algorithm. The laser mask is separated into negative and positive side based on the large central mark and the direction marks. The regions are selected by matching the contours with the region masks. The visible marks on each side are counted, excluding the central large mark and the direction mark.

A method for counting visible laser marks based on the OpenCV image processing library is illustrated in Fig. 4. The region of interest for each side is selected by matching the contour of the whole mask with the negative and positive region masks. The direction mark and large central mark are used to determine the direction and to locate the mark position. Additionally, a laser mark next to the large central mark in the region mask is mandatory for distinguishing the large mark from normal marks.

3.3 Mask classification

Beam defocusing cannot be completely avoided in the process with substantial robot movements in 3D area. The influence of the beam defocusing was studied by applying an ablation process on fused silica. According to the applied F-Theta lens f = 160 mm and the beam quality factor $M^2 = 1.2$, the defined Rayleigh length is calculated to 2.582 mm. Maintaining the standard processing surface (parallel to the ground), the robot moved with an offset step of 200 μ m through the focus offset range of ± 2 mm. After the robot arrived at the corresponding offset, a cavity was ablated. As shown in Fig. 5(a), a negligible variation on the ablation depth is observed within the focus offset range of ±600 μm. Ablation performance in the positive offset direction is more consistent compared to the negative direction. A significant decrease in ablation depth is observed beyond a focus offset of $\pm 1500 \, \mu m$, while a slight reduction occurs

Table 2 Classification of focus offsets.

class	offset range/µm	meaning	
0	$-300 \sim +300$	Optimal for processing	
1	+301~+500	Positive offset acceptable	
2	+501~+800	Positive offset should be corrected	
3	>801	High positive offset	
- 1	$-301 \sim -500$	Negative offset acceptable	
-2	$-501 \sim -800$	Negative offset should be	
3	< 801	High negative offset	

between 600 μm and 800 μm offsets on both sides. In contrast, the surface roughness shows a high sensitivity to defocusing. A notable increase in surface roughness is observed for the offsets exceeding $\pm 400~\mu m$ in both directions.

To ensure robust process capability while maintaining a stable process quality during complex 3D movements, the mask is simplified and categorized into seven classes, as illustrated in Fig. 5(b). The definitions and corresponding meanings of these classes are provided in Table 2.

However, the influence of the utilized F-Theta lens should also be considered. The definition of focus length range is based on the calculated Rayleigh length, e.g. a range of ± 1 mm is recommended for a 100 mm focus length. The offset step is selected based on the focus length range as well as the focus offset classification. The offset step should be able to remain the class distribution shown in Fig. 5(b).

4. Results and discussion

4.1 Mask analysis with image processing-based method

The laser marks with various line numbers and background were captured by the focus camera on the USPLR

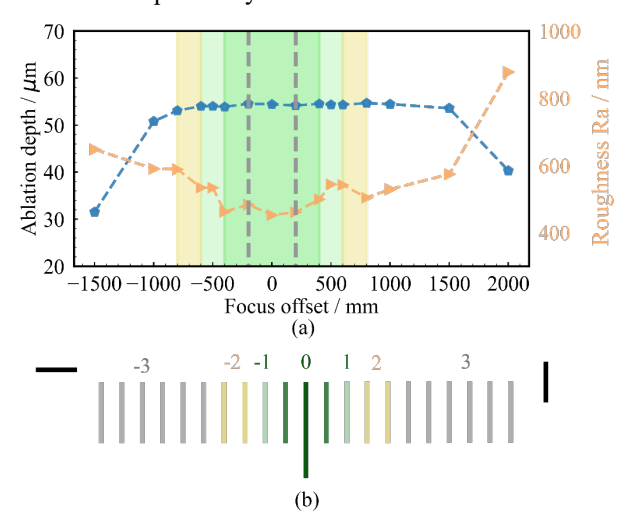


Fig. 5 Mask classification based on the ablation process. (a) The influence of beam defocusing on fused silica ablation using the USPLR system. (b) The mask is categorized as 7 classes, in which the number represents the level of offset and the sign represents the offset direction.

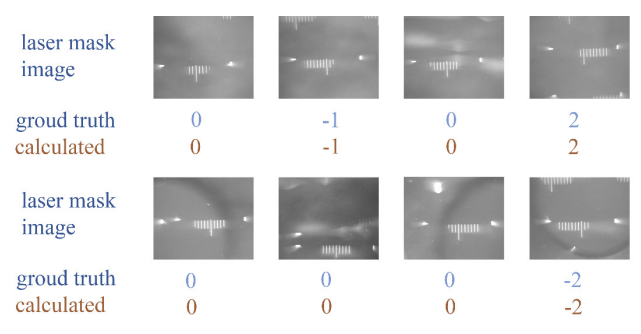


Fig. 6 Examples of laser mask applied for method testing. The variations in the number of laser marks, mark positions and background were considered. The calculated line numbers are rounded to the digit.

system. The proposed method was tested with 37 samples and the calculation accuracy is 94.28% (A part of samples is shown in Fig. 6.).

However, the proposed image processing-based method is sensible to the changing of mark size and orientation and presents a low tolerance on environmental deviation. Furthermore, at least one mark on the side is mandatory for the region detection and the subsequent calculation, which limits flexibility.

4.2 Mask analysis with YOLO-based method

Machine learning models have been widely applied for object detection and classification, which shows a high tolerance of the variation of environment. The YOLO object detection model due to the capability of real time object detection and classification shows the potential on efficient focus classification for the 3D processing using USPLR

Table 3 Training dataset structure.

Real-single	Mixed	Real-double
212	212	424
120	120	120
NA	122	NA
NA	120	NA
332	574	544
	212 120 NA NA	212 212 120 120 NA 122 NA 120

system. Please note that YOLOv7 [29] is applied in the experiment.

For a more general model, the number of total visible marks varies from 6 to 12 for the model training, while the large central mark remains included in the visible mark sequence. The marks are counted separately on each side, starting from the large central mark and extending outward. The number of the total visible marks is calculated as the sum of the visible marks on both sides plus the large central mark excluding the side mark. Please note that class variables increase with the number of total visible masks. A total of 106 sample variables were used, with each sample variable representing a unique combination of the visible mark number and its corresponding classification label.

The dataset structure influences training accuracy. The baseline dataset (Real-single) consists of one item per sample variable, and a 180° rotated version of selected items, the 40 negative samples containing only the background without

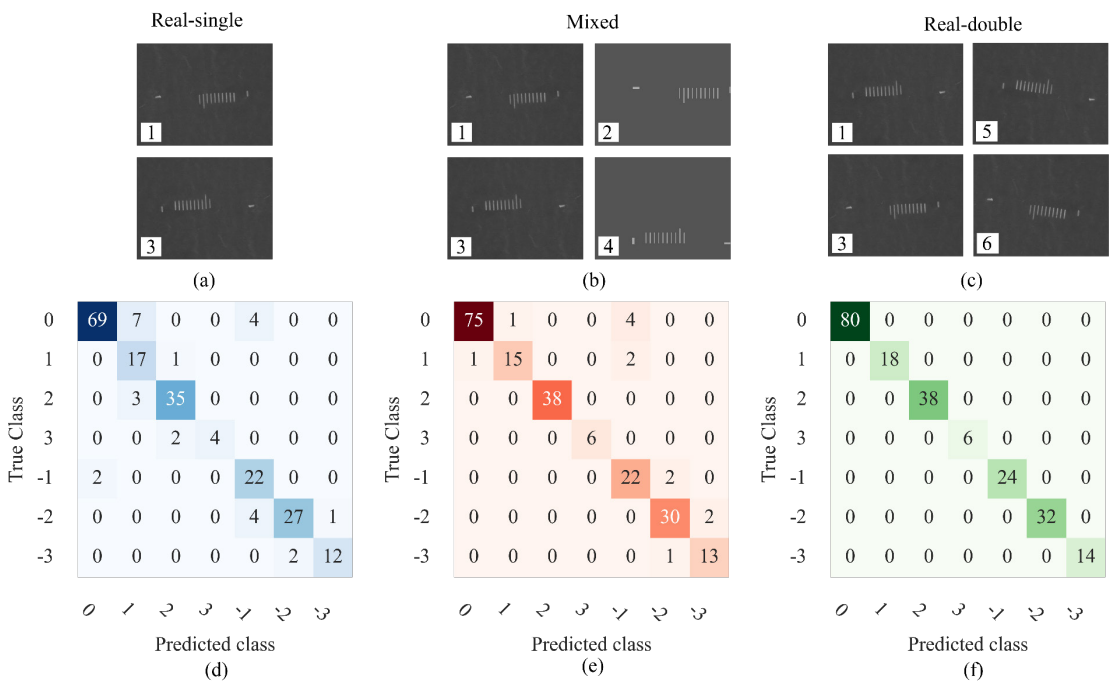


Fig. 7 The structure of training datasets and their corresponding test result. The training data structure for (a) One item per sample variable with pure real data. (b) Mixed of one item from real data and one artificial data. (c) Two items per sample variable with pure real data is shown. (Numbers represent the item with various operation. 1: original item, 2: artificial item; 3: original item rotated of 180°, 4: artificial item rotated of 180°, 5: second original item, 6: second item rotated of 180°.) Confusion matrix of the model trained by the (d) Real-single, (e) Mixed, and (f) Real-double dataset. The number in the confusion matrix represents the applied sample number.

any visible marks (Fig. 7(a)). Given the typically high cost of data generation, additional artificial samples were incorporated to expand the dataset size (Mixed). This database consists of one item per sample variable, one artificial item, and a 180° version for both original and artificial items (Fig. 7(b)). In addition, a dataset composed of pure real data, with two items per sample variables and a 180° rotated version for each item (Real-double), was also used for model training (Fig. 7(c)). The number of applied items in the three datasets is shown in Table 3. For efficient model training with less training samples, a pretrained YOLO7-tiny model was initialized for the training.

An item was randomly selected from each sample variable for the model test. The test dataset consists of the original items, the selected items with a rotation between $\pm 30^{\circ}$ while changing the position randomly, as well as a 180° rotated version. 212 items were used in the experiment.

The test result of the model trained by three datasets is illustrated in Fig. 7(d-f). The Mixed dataset improves the model prediction accuracy with the average prediction accuracy of 93.9%, which is 6.9% higher than the Real-single dataset. Noting that, the prediction accuracy of class 0, 2, 3 and -2 increases using the Mixed dataset. However, wrong prediction was found in class 0 using both Real-single and Mixed datasets, which is the most essential class for the laser processing. In contrast, all the test items were correctly classified using Real-double dataset.

Using the same YOLO model, the model accuracy is improved with increasing training items. Artificial data suppresses the cost of data generation and improves training accuracy. However, artificial data could not replace the real data completely. Remaining the same scale of training dataset size, the model trained by the dataset composed of pure real data shows higher accuracy compared to the artificial data mixed dataset.

4.3 3D ablation processing using USPLR system

Cavities are ablated on fused silica in various surface orientations. Both image processing-based and YOLO-based methods are implemented in the USPLR system. The beam focus monitoring and ablation process with various surface orientations is illustrated in Fig. 8. The processing surfaces are rotated along the y axis with a 15° increment from -30° to 15°. (Please note, the rotation exceeding 15° can result in collision and is therefore out of discussion.) The following steps are performed for each surface rotation:

- 1. The robot moves to the processing area and adjusts the distance using the confocal sensor;
- 2. The scanner writes mask with offsetting focus with a 200 μm step ranging from -2 mm to 2 mm along the normal of processing surface;
- Robot moves camera to the processed position and captures laser mask. The mask is than analyzed by the image processing-based method and the trained YOLObased method;
- 4. A new specimen replaces the processed specimen, following the adjustment of the system to the set distance corrected in the step 3;
- 5. Cavities are ablated with offsetting adjusted beam focus in the range of ± 2 mm along the processing surface normal in a 200 μ m offset step. One cavity is ablated after robot moves an offset step along the processing surface

normal and a 3 mm offset along the y direction. The beam focus is monitored by the confocal sensor before each cavity ablation process.

The test is repeated three times.

The ablation on fused silica at four rotation positions versus focus offset is shown in Fig. 9(a), revealing a constant ablation depth in the focus offset range of $\pm 1000~\mu m$ for all orientations. The average ablation depth is 54.6 μm for dy = 0° and 54.8 μm for dy = -15° in the constant ablation range, while a reduction of 2.1 μm and 2.3 μm of ablation depth is observed at dy = 15° and at dy = -30° as compared to the ablation depth at dy = 0° . The maximum standard deviation of the ablation depth is $1.69~\mu m$ in the offset range of $\pm 1000~\mu m$, which is observed at dy= -30° . Processing stability depends on the system orientation.

Apparently, a large orientation leads to a reduction on the processing stability. The torque increases as Axis6 moves away from the initial position, where a minimum torque between Axis4 and Axis5 presents (at dy = 0°), which in turn compromises system stability and reduces the ablation quality subsequently. Additionally, at a focus offset of 1500 μm , a smaller reduction in ablation depth is found at negative orientations, whereas a significant reduce occurred at dy = 0° and 15°. One assumption for this behavior is the inhomogeneous fluence distribution led by the extremely defocused laser beam (elliptical beam spot form) in conjunction with the axis orientation variation. Furthermore, negative defocusing resulted in a more significant decrease in ablation depth as compared to the positive direction. No ablation is detected at $-2000~\mu m$ offset in the negative direction, while

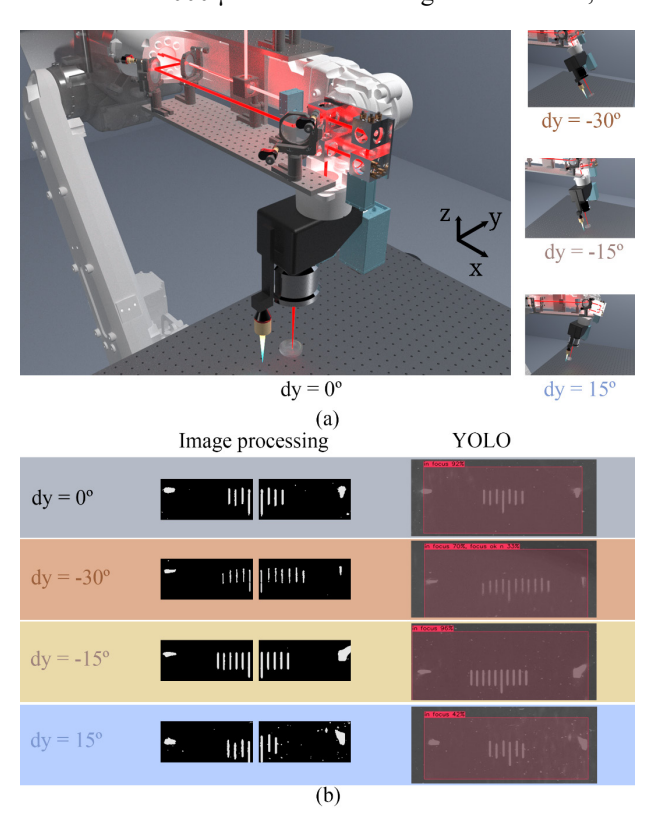


Fig. 8 Illustration of ablation on fused silica with variable surface orientations using USPLR system. (a) Robot system and processing surface rotate along y direction from -30° to 15° with remaining the beam propagating axis behind F-Theta lens parallel to the surface normal. (b) Both methods determine the beam focus correctly at four rotation positions.

an ablation depth of 51.3 μm is achieved at 2000 μm offset with dy=-30°.

Also, the surface roughness R_a exhibits a high sensitivity on beam defocusing (Fig. 9(b)). A low roughness is observed within the focus offset range of $\pm 400~\mu m$. The maximum average roughness for four rotations is about 500 nm with a standard deviation of 43.7 nm within this offset range, which is shown at dy = 0°. Cavities ablated at dy=0° and 15° exhibit a comparable surface roughness trend. Interestingly, negative orientations are found to suppress the surface roughness. A low roughness is observed at negative orientations within the range of 600-1400 μm . This behavior suggests that defocused laser beam with elliptical spot form contributes to surface roughness, and the variations in system orientation can mitigate this effect, offering a possibility to enhance surface quality through optimized surface orientation.

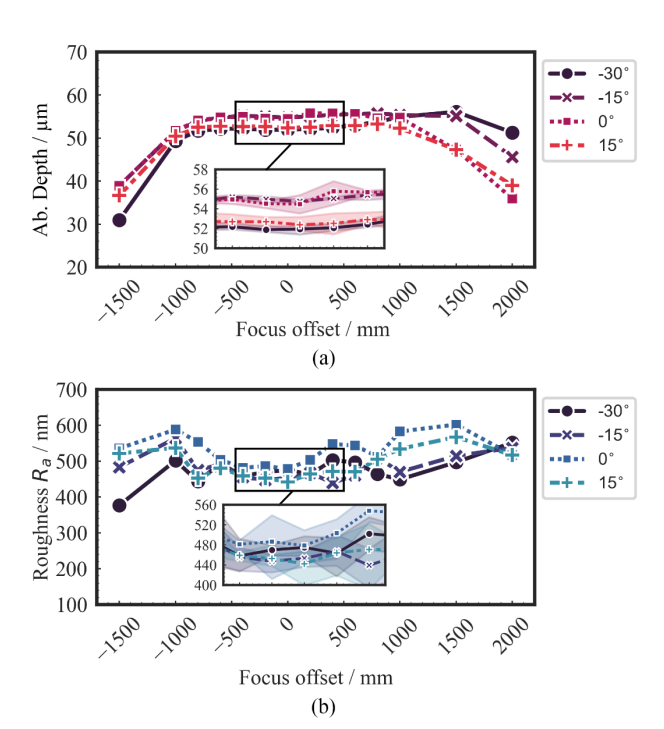


Fig. 9 Average ablation depth and surface roughness R_a with system orientation variation from -30° to 15° . Three cavities were ablated at each offset step. The value in the range of $\pm 400~\mu m$ with the standard deviation.

5. Conclusion

A focus monitoring approach for 3D laser processing using an ultrashort pulsed laser robot system is developed. The system moves along the processing surface, remaining the beam propagating axis behind F-Theta lens parallel to the normal of the processing surface. The beam focus monitoring and adjustment during the process is realized by adjusting the distance between the system and processing surface using a confocal sensor. Methods based on image processing and deep learning YOLO model for laser mark classification are developed, which are applied for focus monitoring and distance correction between system and processing surface. For model training, three training dataset structures are compared, wherein the model trained by the dataset consisting of two items per sample variable plus the 180° rotated version shows the highest accuracy. Both, image-processing based and YOLO-based methods determine the beam focus in the

ablation on fused silica with varying the surface orientation correctly.

Varying surface orientation and beam focus position, cavities are ablated using the USPLR system. The ablation depth is found to be constant while offsetting the beam focus in the range of $\pm 1000~\mu m$. The resulting surface roughness exhibits a high sensitivity on beam defocusing and surface orientation. A constant surface quality is observed in the focus range of $\pm 400~\mu m$ within the surface orientation range of -30° to 15° . An asymmetric reduction in surface roughness is shown with varying surface orientation, where a lower surface roughness is observed at negative surface orientations in the positive focus offsets.

Acknowledgments and Appendixes

This research was funded by the Bavarian Ministry of State for Economy, Land Development and Energy (project RoboSens, grant number DIK0375/01) and by the Bavarian Ministry of Science and Arts (project LEZ, grant number H.2-F1116.AS/34/2).

References

- [1] S. Staehlke; T. Barth; M. Muench; J. Schroeter; R. Wendlandt; P. Oldorf, R. Peters, B. Nebe, and A. Schulz: J. Funct. Biomater., 15, (2024) 34.
- [2] S. Loganathan, G. Sharma, E. Daskalakis, S. Strafford, E. Kumi Barimah, and A. Jha: Adv. Mater. Technol., 10, (2025) 2401362.
- [3] M. Maiuri, M. Garavelli, and G. Cerullo: J. Am. Chem. Soc., 142, (2019) 3.
- [4] M. Ryabikin, M. Emelin, and V. Strelkov: Physics -Uspekhi, 193, (2023) 360.
- [5] C. Lutz, S. Schwarz, J. Marx, C. Esen, and R. Hellmann: Photonics, 10, (2023) 413.
- [6] S. Kefer, J. Zettl, C. Esen, and R. Hellmann: Materials, 15, (2022) 6233.
- [7] K. Jiang, P. Zhang, S. Song, T. Sun, Y. Chen, H. Shi, H. Yan, Q. Lu, and G. Chen: Mater. Sci. Semicond. Process., 180, (2024) 108559.
- [8] L. Li, W. Kong, and F. Chen: Adv. Photon., 4, (2022) 24002.
- [9] J. Zettl, S. Rung, C. Esen, and R. Hellmann: J. Laser Micro Nanoeng., 16, (2021) 42.
- [10] E. Kažukauskas, S. Butkus, V. Jukna, and D. Paipulas: Surf. Interfaces, 50, (2024) 104471.
- [11] H. Wang, C. Pan, C. Li, K. Menghrajani, M. Schmidt, A. Li, F. Fan, Y. Zhou, W. Zhang, and H. Wang: Int. J. Extrem. Manuf., 6, (2024) 42002.
- [12] S. Kefer, G.-L. Roth, J. Zettl, B. Schmauss, and R. Hellmann: Photonics, 9, (2022) 234.
- [13] S. Schwarz, S. Rung, C. Esen, and R. Hellmann: Opt. Express, 29, (2021) 23477.
- [14] M. Mackevičiūtė, J. Dudutis, and P. Gečys: Opt. Lasers Eng., 183, (2024) 108490.
- [15] Y. Yang, K. Bischoff, D. Mücke, C. Esen, and R. Hellmann: J. Laser Appl., 36, (2024) 12019.
- [16] K. Bischoff, D. Mücke, G.-L. Roth, C. Esen, and R. Hellmann: Polymers, 14, (2022) 2962.
- [17] K. Yildirim, B. Nagarajan, T. Tjahjowidodo, and S. Castagne: J. Manuf. Process., 133, (2025) 1126.

- [18] B. Cao, P. Le, S. Ahn, H. Kang, J. Kim, and J. Noh: Opt. Express, 25, (2017) 28427.
- [19] B. Cao, P. Le Hoang, S. Ahn, J. Kim, and J. Noh: Precis. Eng., 50, (2017) 204.
- [20] J. Du, F. Li, F. Peng, S. Wang, and W. Yan: Opt. Express, 30, (2022) 6981.
- [21] A. Voulodimos, N. Doulamis, A. Doulamis, and E. Protopapadakis: Comput. Intell. Neurosci., 2018, (2018) 7068349.
- [22] M. Shehryar Khan, S. I. Shahabad, M. Yavuz, W. W. Duley, E. Biro, and Y. Zhou: J. Manuf. Process., 67, (2021) 535.
- [23] J. Redmon, S. Divvala, R. Girshick, and A. Farhadi: Proc. IEEE conf. on computer vision and pattern recognition 2016, 779.
- [24] J. Jiang, X. Fu, R. Qin, X. Wang, and Z. Ma: Remote Sens., 13, (2021) 1909.
- [25] Y. Zhou: Expert Syst. Appl., 238, (2024) 122256.
- [26] D. Franz, Y. Yang, L. Michel, C. Esen, and R. Hell-mann: J. Laser Appl., 35, (2023) 42057.
- [27] Y. Yang, D. Franz, C. Esen, and R. Hellmann: J. Laser Appl., 35, (2023) 42039.
- [28] Y. Yang, D. Franz, C. Esen, and R. Hellmann: J. Intell. Manuf., (2025). https://doi.org/10.1007/s10845-025-02595-4
- [29] C.-Y. Wang, A. Bochkovskiy, and H.-Y. M. Liao: "YOLOv7: Trainable bag-of-freebies sets new state-of-the-art for real-time object detectors", (Jul. 2022. [Online]. Available: http://arxiv.org/pdf/2207.02696v1

(Received: June 5, 2025, Accepted: November 24, 2025)